doi:10.26443/seismica.v4i1.1444

SEISMICA

Quantifying Rotation-Induced Errors in Near-Field Seismic Recordings: Assessing Impact on Rotation and Acceleration Measurements

Yara Rossi * [1,2], **Felix Bernauer** [1], **Chin-Jen Lin** [3], **Frédéric Guattari** [4], **Baptiste Pinot** [5]

[1]Department of Earth and Environmental Sciences, Ludwig-Maximilians Universität in München, Munich, Germany, [2]Department of Earth Sciences, University of Oregon, Eugene, USA, [3]Institute of Earth Sciences, Academia Sinica, Taipei, Taiwan, [4]MAÅGM, Le Mans, France, [5]Institut Supérieur de l'Aéronautique et de l'Espace (ISAE-SUPAERO), Toulouse, France

Author contributions: *Conceptualization*: Rossi Yara, Bernauer Felix, Chin-Jen Lin. *Methodology*: Rossi Yara, Bernauer Felix, Frédéric Guattari, Baptiste Pinot. *Formal Analysis*: Rossi Yara. *Writing - Original draft*: Rossi Yara. *Writing - Review & Editing*: Rossi Yara, Bernauer Felix, Chin-Jen Lin, Frédéric Guattari, Baptiste Pinot. *Visualization*: Rossi Yara. *Funding acquisition*: Rossi Yara.

Abstract Recent development of rotational seismometers allows for detailed measurements of wave field gradients, providing information previously unattainable. Knowledge about the full wavefield is imperative to understand sensor errors from ground-motion. It is well-known from navigation solutions that rotational data requires proper processing to be physically meaningful. This study focuses on investigating and quantifying two errors affecting the recording of rotations: 1) misorientation of the sensor to the local coordinate system called attitude error and 2) changing projection of the Earth's spin in the sensor coordinate system - Earth's spin leakage. Using 6-component datasets, 3C translation and 3C rotation, from near-field events at the Kīlauea Caldera in Hawaiʻi and the Mw 7.4 Hualien event on 2024-04-02, we perform a rotation-correction for the 6C data. We find that the Earth's spin leakage is negligible for rotations, while the attitude error of rotations increases with ground-motion amplitude, potentially becoming significant for large earthquakes in the near-field. The errors on the rotation sensor do not significantly affect corrections of accelerations in our dataset. However, they may be relevant for high-amplitudes or in highly sensitive applications. This work offers the first quantification of these errors in seismology and provides guidance for corrections in future studies.

Production Editor:
Yen Joe Tan
Handling Editor:
Paula Koelemeijer
Copy & Layout Editor:
Aisling O'Kane

Received:
September 10, 2024
Accepted:
May 14, 2025
Published:
June 17, 2025

1 Introduction

Seismic waves propagating through the subsurface not only include the traditionally measured translations such as displacement, velocity, or acceleration, but consists of a variety of additional motion types namely rotation and strain. These additional degrees of freedom contain the gradient information of the wave field, that can help identify the direction of the propagating waves, i.e. the back azimuth (Yuan et al., 2021), the source mechanism (Ichinose et al., 2021) or subsurface imaging (De Ridder and Curtis, 2017). Today's seismic instrumentation allows tracking of all 12 components (12C) of motion: 3C translation, 3C rotation, and 6C strain. However, this neither holds for the full frequency spectrum nor for the full amplitude range. Every instrument has limitations that must be considered, and even if the instrument records reality correctly, it doesn't only record the signal we are interested in. Corrections therefore, have to be applied to remove these broadly defined errors.

In recent years, a variety of rotation sensors have made it to the experimental stage or even on the market for sale. This has been an important step forward to be able to verify the theoretically-known wave field. The traditional way of observing seismic waves only through 3C translations is a simplification, as 3/4 of the information is not being tracked. This has proven problematic in the case of rotation-induced errors on traditional sensor systems, which derive from a change of orientation of the sensor to the local coordinate system (Crawford and Webb, 2000; Graizer, 2006). There have also been studies on how the tilt and torsion influence accelerometers by analysing experimental data from robot induced motion (Lin et al., 2010; Rossi et al., 2021). These studies showed that gravitational leakage, attitude error of translations, and inertial acceleration are induced by rotations, falsifying the recorded acceleration data. Studies using translational broadband seismometers in ocean bottom and volcanic environments found that there might be substantial error due to the tilt of the sensors (Lindner et al., 2017; Bernauer et al., 2020). However, corrections for rotation-induced inertial forces have not yet been applied to seismic recordings and will not be covered in this study either. In addition, the influence of antenna pole tilting on the estimated displacement from GNSS data was studied in a robot arm experiment in Rossi et al. (2021). The study showed that, depending on the application, this error could potentially be significant to demand a post-processing correction. Nonetheless, we will not cover

*Corresponding author: rossi.yara@outlook.com

GNSS rotation-correction in this study. Kalman filter-based real-time applicable rotation-correction schemes have been developed by Geng et al. (2019) and Rossi et al. (2021, 2024). The main theory of these correction and fusion schemes are derived directly from navigation solutions (Kalman, 1960).

All the above mentioned rotation-correction schemes rely heavily on rotational data, underlining the need for precise angle information. The quality of the rotational sensors has to be comparable to the translational sensors, to avoid introducing new errors deriving from sensor self-noise. Through the development and analysis of new rotational sensors such as FOSREM (Kurzych et al., 2016), Eentec-R1 (Bernauer et al., 2012), blueSeis-3A (Bernauer et al., 2018), Rotaphone (Brokesova and Malek, 2013) and Quartz Rotation Sensor (Venkateswara et al., 2021), data availability for seismic, explosive and volcanic ground-motion as well as datasets from building monitoring has increased. An extensive comparison of some of these sensors, focusing on self-noise levels and recording stability over time, has been performed in Bernauer et al. (2021). However, the rotations that induce errors on translational sensors, also influence the rotation recordings. The correction schemes for these errors are derived from navigation theory and are in fact quite elegant (Draper, 1981; Diebel, 2006). The rotation-induced errors on rotation sensors are corrected using the data recorded by the sensor itself. While this approach may initially appear to be circular, it is effective and is routinely implemented in navigation solutions (Savage, 2000; Hasan et al., 2009). The first error is the attitude error of the rotations which can be corrected using the attitude equation to relate the observed rotation angles in the body system to the Euler angles defined in the local system (Euler, 1775; Savage, 2000). This has been applied for seismic experiments on a robot arm in Lin et al. (2010). The second error is due to the spinning Earth. The rotation rate of the Earth is measured by the sensor, but through the dynamic rotation of the sensor, the projection of the Earth's spin onto the xyz-axis of the sensor will change. This error is not to be confused with the Coriolis effect that affects translational accelerometers due to the Earth's spin. The magnitude of the two rotation-induced errors on the rotational sensor remains uncertain, and it is not yet determined whether correction is necessary in all cases, in specific instances, or not at all.

In this study, we provide the first quantification of the two rotation-induced errors on the rotational sensor - attitude error and Earth's spin leakage, offering seismologists an estimate of the error magnitude and guidance on whether a correction is necessary. Additionally, we analyse whether these errors affect two rotation-corrections for accelerometers, namely attitude error of translations and gravitational leakage, and quantify the resulting impact. To accomplish this, we are using the only two 6C datasets that exist globally that captured near-field ground-motion, 1) the earthquakes and summit collapses from the 2018 eruption series at the Kīlauea Caldera, Hawai'i and 2) the Mw 7.4 in Hualien, Taiwan on 2024-04-02.

2 Data

In this study two different datasets were used. The first consists of multiple earthquakes recorded at one station location on the Island of Hawai'i. Two sensors were short-term deployed in the Uwekahuna station vault, of the Hawaiian Volcano Observatory monitoring network at the Kīlauea Caldera on the Island of Hawai'i. The rotational data was recorded by a blueSeis-3A by exail (former iXblue), which is unfortunately a discontinued product line. The accelerometer was a Kinemetrics EpiSensor recorded on a Kinemetrics Quanterra Q330 digitizer. The rotation sensor was set up due to an ongoing volcanic eruption that lasted from May to August 2018. It was initially published in Wassermann et al. (2020) and rotation-correction algorithms for rotation-induced errors on the accelerometer were tested in Bernauer et al. (2020). This dataset is unique, as it provides the only near-field recordings of rotational ground-motion, including three summit collapses with Mw 5.3 and thousands of smaller earthquakes up to Ml 4.36 within 3 km of the station location. Although the two sensors were placed in the same vault they were not on the same pier, potentially causing a difference in the shaking history as described in Wassermann et al. (2020). The five Hawai'i events discussed in this paper are summarised in Table 1 and shown on Figure 1(a).

The second dataset consists of the Mw 7.4 earthquake recorded at two station locations in eastern Taiwan. On the 2nd April 2024, Hualien was struck by a Mw 7.4 reverse fault near the Eurasia and Philippine Sea plate boundary (U.S. Geological Survey, 2024). The earthquake was recorded by rotational sensors at two station locations, where one of the two, MDSA0, is located directly above the largest slip, as seen in Figure 1 (b). Station MDSA0, located in a 0.5 m-deep vault in Hualien, consists of an eaxil blueSeis-3A rotational sensor, a collocated Nanometrics Titan accelerometer and is recorded on a Reftek Wrangler digitizer (Ma et al., 2024). The other station, NA01, is located in a 2 m-deep vault in Nanao and consists of an exail blueSeis-3A rotational sensor, a collocated Kinemetrics EpiSensor ac-

Location	Event type	Time	Magnitude	Depth	Distance from station	Station
Hawai'i	Earthquake	2018-07-12T05:12:41	3.18 ml	<1 km	2.9 km	UWE
Hawai'i	Earthquake	2018-07-14T04:13:33	4.36 ml	<1 km	1.6 km	UWE
Hawai'i	Summit collapse	2018-07-13T00:42:27	5.3 mw	<1 km	3 km	UWE
Hawai'i	Summit collapse	2018-07-14T05:08:04	5.3 mw	<1 km	3 km	UWE
Hawai'i	Summit collapse	2018-07-15T13:36:05	5.3 mw	<1 km	2 km	UWE
Taiwan	Earthquake	2024-04-02T23:58:12	7.4 mw	0-45 km	directly below	NA01, MDSA0

Table 1 Six events used within this study.

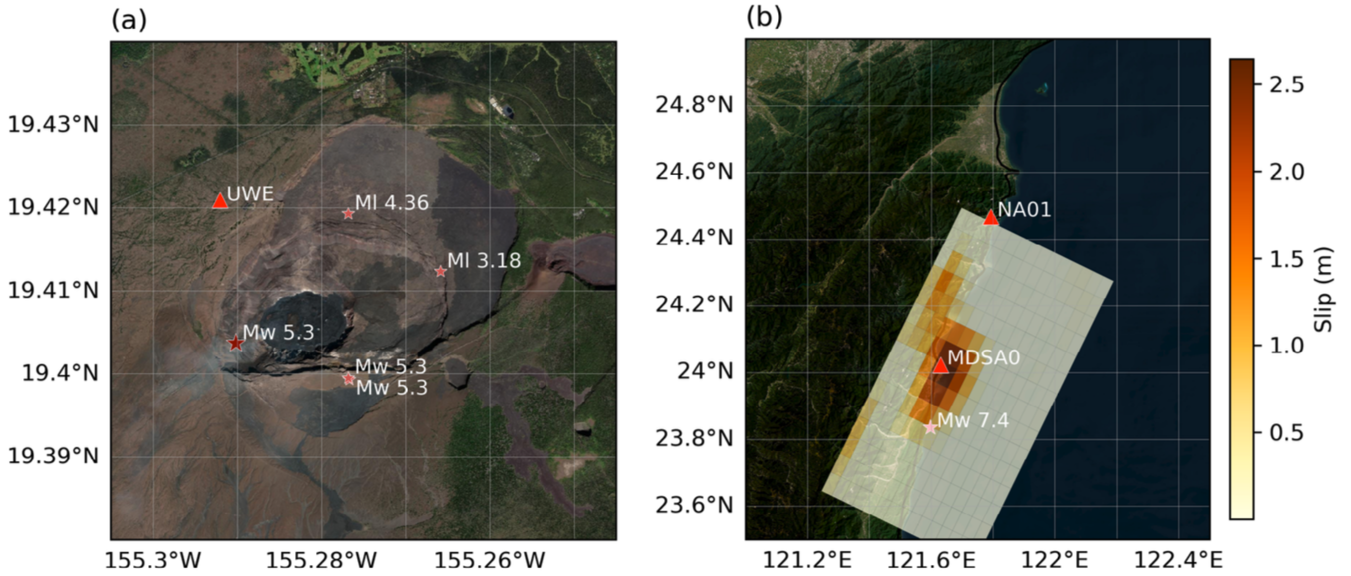

Figure 1 Summary of the station and event locations used in this publication. In (a) the Kīlauea Caldera is shown with the two earthquakes and three summit collapses denoted as stars. The dark red star marks the location of the Mw 5.3 event, shown as a time series in this publication. In (b) the Hualien event in Taiwan is shown. The epicenter is marked with a light red star. The fault rupture has a length of 35 km going north of the epicenter. The station MDSA0 is on top of the rupture fault patch U.S. Geological Survey (2024).

celerometer, and is recorded on a Kinematics Quanterra Q330 digitizer (Yuan et al., 2021; Chen et al., 2023). The locations are noted in Figure 1(b), while the event details are noted in Table 1.

3 Method

Three coordinate systems are used in this paper: body, local, and global, and are visualized in Figure 2. The body system 'B' is fixed to the instrument measuring the sought after quantities, with the origin at the center of the sensor. The seismic ground-motions are defined within the local system 'L' (also called the topographic coordinate system), that has the origin at the initial instrument location at the Earth's surface and is oriented according to East, North, and Up. The global system 'G' is defined as the Earth-centered inertial coordinate system in Latitude and Longitude, which has the origin at the Earth's center and is fixed with respect to the stars. All three systems have positive rotation according to the right-hand rule. We are interested in two levels of dynamic rotation corresponding to two rotation errors on rotation sensors; 1) the rotation of the body frame in the local frame, and 2) the rotation of the local frame in the global frame:

1. The body system will change both orientation and location within the local system during seismic ground-motion. The rotations measured by a rotational seismometer are true only within their own frame 'B' (body system), whereas seismologists are interested in the ground-motion in the local system 'L' defined by East, North, and Up. The error on the rotational sensor derived from this effect is called attitude error in this study.
2. The local system is fixed at a point on the surface of the Earth and rotates with it. Therefore, the local system rotates around the global system at the speed of the Earth's rotation around the North axis. The error on the rotational sensor derived from this effect is called the Earth's spin leakage in this study.

3.1 Attitude error of rotations

Through dynamic rotational motion of the body system, the axes in the body frame are no longer oriented according to the axes of the local frame. In other words, if we have a rotation around the y-axis, the rotation measured around the x-axis will no longer point in the East direction. This effect is called attitude error. To get the equivalent measurements in the local system, a coordinate system transformation has to be applied to the rotation rates $\dot{\boldsymbol{\theta}}$ observed in the body system using Equation 1 (Savage, 2000). This is a well known conversion to correct for the attitude error in navigation, but has only recently been applied for seismic applications (Lin et al., 2010). The transformation matrix $\mathbf{A}$ (Equation 2) is used to transform $\dot{\boldsymbol{\theta}}$ into the equivalent Euler rotation rate $\dot{\boldsymbol{\Psi}}^{euler}$ in the local system.

$$\dot{\boldsymbol{\Psi}}^{\text{euler}} = \begin{bmatrix} \dot{\Psi}_e \\ \dot{\Psi}_n \\ \dot{\Psi}_z \end{bmatrix}^{\text{euler}} = \mathbf{A} \cdot \dot{\boldsymbol{\theta}} = \mathbf{A} \cdot \begin{bmatrix} \dot{\theta}_e \\ \dot{\theta}_n \\ \dot{\theta}_z \end{bmatrix} \tag{1}$$

$$\mathbf{A} = \begin{bmatrix} 1 & s_e \tan(\Psi_n) & c_e \tan(\Psi_n) \\ 0 & c_e & -s_e \\ 0 & s_e \sec(\Psi_n) & c_e \sec(\Psi_n) \end{bmatrix} \tag{2}$$
$$with\ c_e, s_e : \cos(\Psi_e), \sin(\Psi_e)$$

The angles used within $\mathbf{A}$ in Equation 1 are Euler angles $\boldsymbol{\Psi}^{euler}$ and not the observed angles in the body

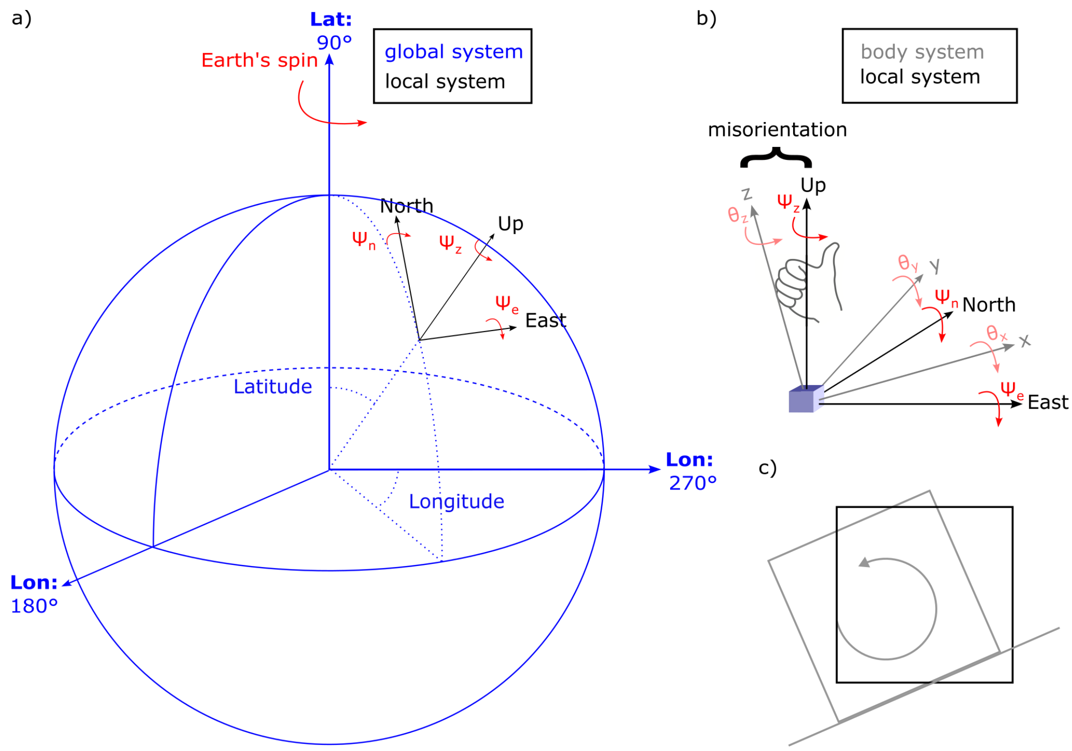

Figure 2 Notation of global, local, and body system for the attitude correction of the rotation sensor. a) shows the orientation of a local system in East, North, Up within the global system, defined through Latitude and Longitude. b) shows how the body system can be misoriented within the local system. The angles relating the body frame to the local frame around the three commonly defined axes of z (yaw), y (pitch), and x (roll) are called Euler angles. The Euler angles, $\boldsymbol{\Psi}$, are located in the local system, and the observed angles $\boldsymbol{\theta}$ are located in the body system. c) is a schematic drawing of a rotational sensor defined in the body system, being misoriented from its initial orientation in the local system.

frame. Additionally, Equation 1 does not take into account the Earth's spin. The full derivation of the Equation 1 is shown in Lin et al. (2010) and therefore not provided again.

3.2 Earth's spin leakage

An absolute rotation sensor is sensitive to the direct current (DC), i.e. static rotation rate. This means that with a high enough resolution it will be sensitive to Earth's spin. Consequently, its data will exhibit an offset corresponding to the projected Earth's spin on each component, depending on its attitude. However, the Earth's spin affects a rotational sensor independently of its sensitivity to DC. This is because the changing projection of the Earth's spin as the sensor rotates with respect to the local system - due to an earthquake for example - has the frequency range of the sensor's motion. So each rotational sensor has to be corrected for the false projection of the Earth's spin into the body system - Earth's spin leakage. A sensor located at the North pole will record the spin only on the z-axis while a sensor at the Equator will record only on the y-axis. With Equation 3, the projection of the Earth's spin in the global system 'G' into the local system 'L' at a specific latitude is calculated.

$$\dot{\mathbf{r}}_{Earth,L} = \begin{bmatrix} 0 \\ \sin(Latitude) * \dot{r}_{Earth,G} \\ \cos(Latitude) * \dot{r}_{Earth,G} \end{bmatrix}, \quad (3)$$
$$with\ \dot{r}_{Earth,G} = 7.2921 \cdot 10^{-5} rad/s$$

The dynamic rotational motion of the sensor due to an earthquake will change the orientation of the sensor to the axis of Earth's spin. This can be corrected as shown in Equation 4.

$$\dot{\boldsymbol{\Psi}}^{spin} = \dot{\boldsymbol{\theta}} - \mathbf{T} \cdot \dot{\mathbf{r}}_{Earth,L} \quad (4)$$

The rotation matrix $\mathbf{T}$ is defined in Equation 5, where $c_e, s_e, c_n, s_n, c_z, s_z : \cos(\Psi_e), \sin(\Psi_e), \cos(\Psi_n), \sin(\Psi_n), \cos(\Psi_z), \sin(\Psi_z)$. $\mathbf{T}$ dynamically calculates the projection of the Earth's spin $\dot{\mathbf{r}}_{earth,L}$ in the local system 'L' according to the motion of the sensor using the 123-Euler transformation according to Diebel (2006). The angles used within $\mathbf{T}$ in Equation 4 are the Euler angles $\boldsymbol{\Psi}^{spin}$.

$$\mathbf{T} = \begin{bmatrix} c_n c_z & c_n s_z & -s_n \\ s_e s_n c_z - c_e s_z & s_e s_n s_z + c_e c_z & c_n s_e \\ c_e s_n c_z + s_e s_z & c_e s_n s_z - s_e c_z & c_n c_e \end{bmatrix} \quad (5)$$

Equation 6 combines both the attitude error and the Earth's spin leakage correction and is provided in continuous form. This allows us to provide rotation rates of the signal alone defined as $\dot{\boldsymbol{\Psi}}^{signal}$.

$$\dot{\boldsymbol{\Psi}}^{signal} = \mathbf{A} \cdot \dot{\boldsymbol{\theta}} - \mathbf{T} \cdot \dot{\mathbf{r}}_{Earth,L} \quad (6)$$

For a real-time implementation the discrete form is supplied in Equation 7, where $\boldsymbol{\Psi}^{signal}_{k=0} = [0, 0, 0]$. Note that Equation 7 is an approximation, because it is equivalent to assuming that the axis of the local frame is not rotating between $k-1$ and k. In navigation, more efficient algorithms have been developed, especially for

$$\mathbf{\Psi}_k^{signal} = \begin{bmatrix}\Psi_e\\ \Psi_n\\ \Psi_z\end{bmatrix}_k^{signal} = \begin{bmatrix}\Psi_e\\ \Psi_n\\ \Psi_z\end{bmatrix}_{k-1}^{signal} + dt \cdot \left(\mathbf{A}_{k-1}^{\Psi_{k-1}^{signal}} \begin{bmatrix}\dot{\theta}_x\\ \dot{\theta}_y\\ \dot{\theta}_z\end{bmatrix}_{k-1} - \mathbf{T}_{k-1}^{\Psi_{k-1}^{signal}} \cdot \dot{\mathbf{r}}_{Earth,L} \right) \tag{7}$$

integrated real time systems (Savage, 2000, Chapter 7), but the computing error between Equation 7 and a more rigorous expression is assumed negligible if the sampling interval is very small. This algorithmic discussion is therefore not the subject of this work.

3.3 Angle Notation

To compare the different correction schemes we define four angles summarized in Table 2. The observed rotation angle $\dot{\boldsymbol{\theta}}$ defined within the body system, has to be demeaned before integration. This is due to the fact that the Earth's spin is generally recorded on all three axes - including the East direction due to small misorientation from the deployment and consequent earthquakes. This is done by subtracting the pre-earthquake mean from the full time series as in Equation 8.

$$\dot{\boldsymbol{\theta}}_{demeaned} = \dot{\boldsymbol{\theta}} - mean(\dot{\boldsymbol{\theta}}_{pre\ EQ}) \tag{8}$$

The angles derived thereof will be called 'rot.' in following sections. The next are Euler angles where the correction for attitude error is applied to $\dot{\boldsymbol{\theta}}_{demeaned}$ without correcting for the Earth's spin leakage, denoted by 'attitude error rc.'. To allow an analysis of the Earth's spin leakage individually, we also provide the demeaned observed rotation angles corrected only for the Earth's spin and not applying the correction for the attitude error, denoted 'rot. + spin rc.'. The last angle represents the full correction including demeaning, attitude error and Earth's spin leakage, which is denoted 'attitude error + spin rc.' and corresponds to $\mathbf{\Psi}_{signal}$ from Equation 7.

3.4 Attitude error of translations and gravitational leakage

As a next step we use the different angles to correct for two rotation-induced errors on the accelerometer sensor, i.e. attitude error of translations and gravitational leakage. The rotation-correction is applied at every time step k through the rotation matrix T defined in Equation 5. The angles $\Psi_e^k, \Psi_n^k, \Psi_z^k$ are defined in each time step k and stand for the 'attitude error + spin rc.' angles as derived in Equation 7. These can be replaced by the 'rot.', 'rot. + spin rc.' and 'attitude error rc.' angles to analyse the difference resulting from using different rotation-corrections for the angles. Matrix T is then used to correct the accelerations at each time step k through Equation 9. Note that Equation 9 corrects both attitude error of translations and gravitational leakage simultaneously, and assumes that the observed acceleration time series do not include gravitational acceleration.

$$\mathbf{a}_{rc}^k = (\mathbf{T}^k \cdot (\mathbf{a}^k + \mathbf{g})) - \mathbf{g}, \quad with\ \mathbf{g} = \begin{bmatrix}0 & 0 & 9.81\frac{m}{s^2}\end{bmatrix} \tag{9}$$

3.5 Acceleration and Displacement Notation

We define five types of accelerations to analyse the rotation-correction using the four different angles (Table 3). The first are the observed and demeaned accelerations defined within the body system without any rotation. Even though the accelerometers used within this study theoretically record zero mean on all three axes when at rest, it is normal to have small static misorientation errors from the deployment and consequent earthquakes or even temperature variation. So the pre-earthquake mean is subtracted from the full time series and will be called 'obs. demeaned' in the following sections. The last four types of accelerations are corrected for the rotation-induced attitude error of the translations and gravitational leakage using one of the four angles defined in Section 3.3. The new accelerations derived are therefore called 'rc. rot.', 'rc. attitude error rc.', 'rc. rot. + spin rc.' and 'rc. attitude error + spin rc.'. The displacements derived through double integration have equivalent names.

4 Results

We apply the attitude error and Earth's spin correction to events recorded at Kīlauea volcano in Hawaiʻi and to recordings of the Mw 7.4 earthquake in Hualien,

Type of Angle	Corrected Error	Correction Scheme	Equation	Variable
'rot.'	-	demean	8	θ_{demeaned}
'attitude error rc.'	attitude error	demean attitude correction	1	$\mathbf{\Psi}^{\mathbf{euler}}$
'rot. + spin rc.'	Earth's spin leakage	demean Earth's spin correction	4	$\mathbf{\Psi}^{\mathbf{spin}}$
'attitude error + spin rc.'	attitude error Earth's spin leakage	demean attitude correction Earth's spin correction	6 and 7	$\mathbf{\Psi}^{\mathbf{signal}}$

Table 2 The two rotation-induced errors on the rotation sensor can be applied separately or combined. This table summarises the notation of these three variations or demeaning in column 1. Additionally, the type of error and the correction scheme is noted, as well as the Equation used and the name of the variable.

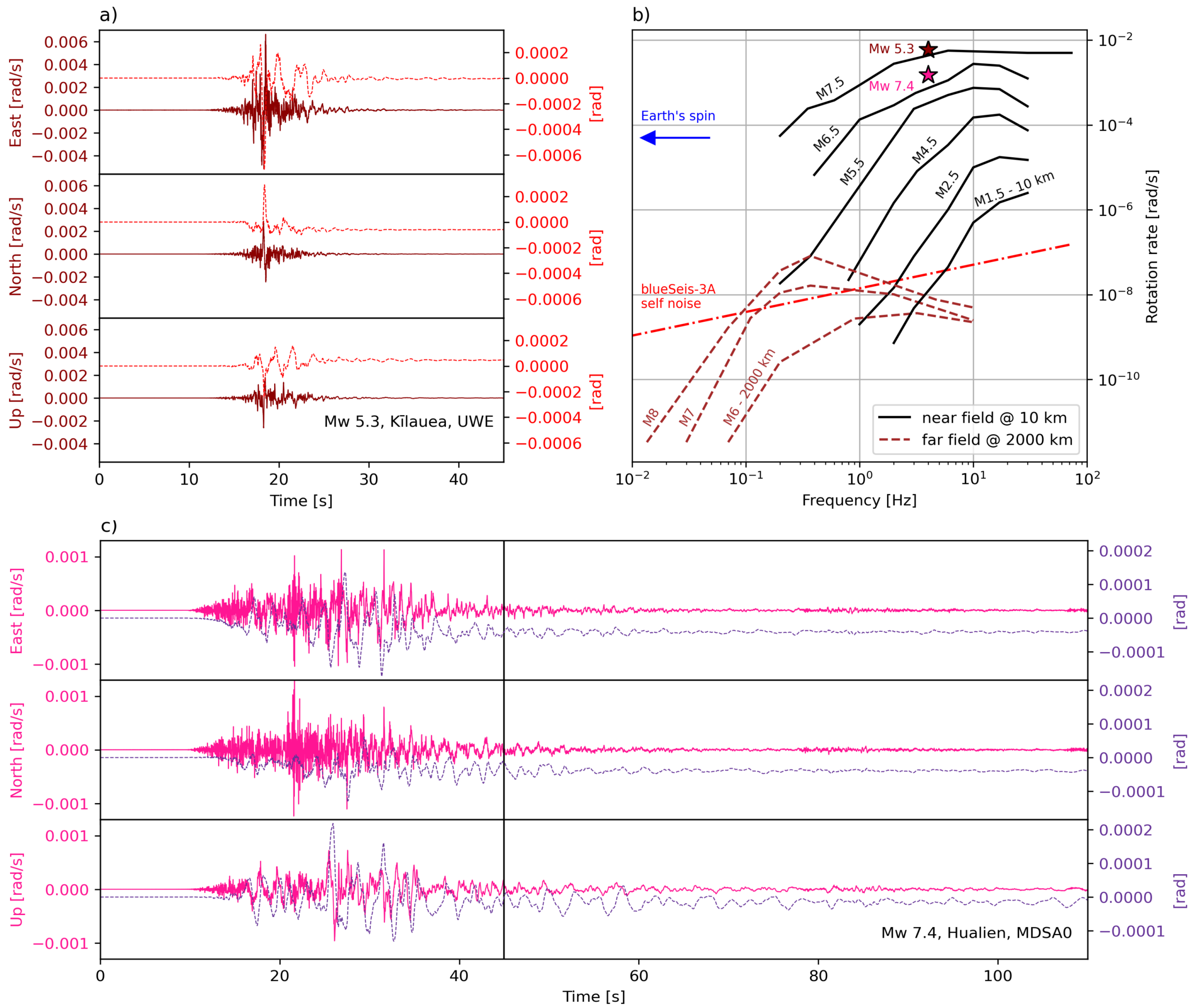

Figure 3 Timeseries of two large earthquakes and the peak rotation rate amplitude from global earthquakes. (a) shows the unfiltered and demeaned time series of rotation angle (dashed, right axis) and rotation rate (solid, left axis) for a Mw 5.3 summit collapse at 2018-07-13T13:26:05 UTC in Kīlauea, Hawaiʻi. (b) is updated from Rossi (2023), which was based on Clinton and Heaton (2002), showing the rotation rate amplitudes of global earthquakes for the near and far field. Additionally, the peak rotation rate amplitudes of the Mw 5.3 (dark star) and the Mw 7.4 (light star) events are shown in perspective to global earthquakes (dashed and solid lines), the sensor self noise (dashed dotted) and Earth's spin (arrow). (c) shows the unfiltered and demeaned time series of rotation angle (dashed, right axis) and rotation rate (solid, left axis) for Station MDAS0 during the Mw 7.4 earthquake at 2024-04-02T23:58:12 UTC in Hualien, Taiwan.

Type of Translation	Angle for Correction	Equation
'obs. demeaned'	-	-
'rc. rot.'	'rot.'	9
'rc. attitude error rc.'	'attitude error rc.'	9
'rc. rot. + spin rc.'	'rot. + spin rc.'	9
'rc. attitude error + spin rc.'	'attitude error + spin rc.'	9

Table 3 All four angles defined in Table 2 are used separately for the rotation-correction of the accelerations. This table links the notation for acceleration and the angles used for the rotation-correction. As provided in column 3, the same Equation is used for all corrections.

Taiwan. We have to iterate again, as shown in study Wassermann et al. (2020) for the Kīlauea events; the rotation and acceleration data do not perfectly match even though the sensors are only 1 meter apart. This slight difference is also visible in our results, so that a perfect rotation-correction cannot be applied. However, as the amplitudes are in the correct range we can give an estimate of the potential error. We would expect to drastically reduce the drift in the low-frequency displacement timeseries through rotation correction of the gravitational leakage. However, the rotation-correction scheme sometimes makes the data worse in the examples shown in the supplementary material (see Figures S1-S8). Even in the Hualien recordings we see that the rotation-corrections do not always reduce the drift (see

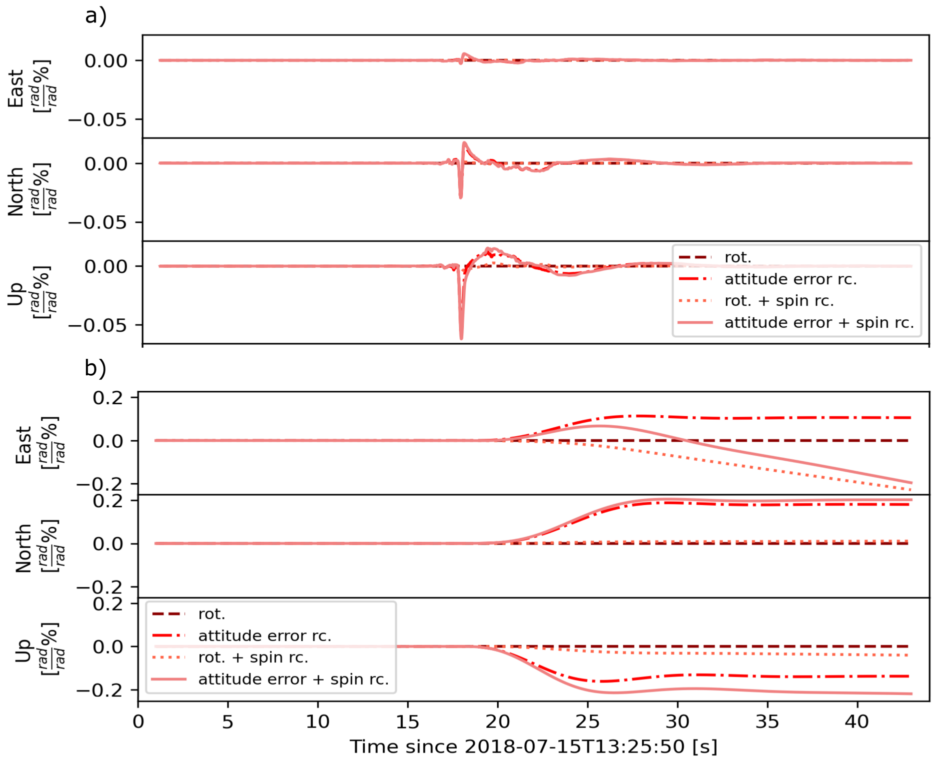

Figure 4 Difference between the three rotation-correction schemes ('attitude error rc.', 'rot. + spin rc.', and 'attitude error + spin rc.') and the observed angles 'rot.' for the Mw 5.3 summit collapse at 2018-07-15T13:35:50 UTC. This is shown in percent of the peak observed angle on that component. (a) shows the high frequencies (0.1 - 25 Hz) and (b) shows the low frequencies (DC - 0.1 Hz).

Figures S9-S12), however it works better than for the Kīlauea events. This is probably due to the fact that in Taiwan the instruments are on the same concrete slab.

The rotation time series of two events are shown in Figure 3; the Kīlauea Mw 5.3 summit collapse on 13_{th} July 2018 (Figure 3a) and the Mw 7.4 earthquake in Hualien on 02^{nd} April 2024 at station MDSA0 (Figure 3c). Figure 3b shows an updated version of the global rotation rate amplitude (Figure 1.2 in Rossi, 2023). The amplitudes derived from global earthquake magnitudes for the near-field or far-field are calculated from Clinton and Heaton (2002), taking advantage of the relationship between acceleration and rotation rate $\dot{\Psi}_z = \frac{a_x}{v_R}$ (Pancha et al., 2000; Sollberger et al., 2018) where V_R is the Rayleigh wave phase velocity. The distances in Clinton and Heaton (2002) were 2000 km and 10 km, and there were unfortunately no results for 1 km distances corresponding to our Hawai'i events. However, Brotzer et al. (2025) predict a peak rotation rate of $10^{-2}\ rad/s$ for a Mw 5.3 event, consistent with what we see here.

The conversion from rotation angles to Euler angles (Equation 1) is influenced by four factors; 1) component of interest xyz, 2) motion on other components, 3) frequency content, and 4) amplitude. The Earth's spin leakage (Equation 4) is additionally influenced by 5) latitude of station. Table 2 lists the details on each rotation correction for the rotation sensor. For this reason we will always show all three components in two frequency ranges, low frequency DC - 0.1 Hz and high frequency - 0.1 Hz to 25 Hz. The different rotation-correction schemes will be shown for an example event; the summit collapse Mw 5.3, shown in Figure 3a. To focus on the influence due to various corrections, we show the time series difference between the angles 'rot.' and the corrected data in Figure 4. The error for both the lower and the higher frequencies is small. However, for this event the correction for the attitude error rendering Euler angles has a larger influence than the Earth's spin leakage correction 'spin rc.'. The largest error for 'attitude error rc.' and 'attitude error + spin rc.' is 0.06% at $17\ s$ for the high frequencies, while the error peaks at 0.2% between $18 - 30\ s$ for the lower frequencies. This matches with the energy timing of the angles themselves.

We apply a scaling technique to allow us to compare ground-motion amplitudes that are smaller than our sensors can measure with ground-motion amplitudes, that are larger than the Mw 7.4 we recorded. For this processing, we chose a Ml 3.18 from Kīlauea (see Table 1) and scaled the ground motion amplitude of the earthquake to match a theoretical M1 to M9 at 10 km distance according to Figure 3b. For each of these new scaled earthquakes, the two angles 'attitude error rc.' and 'rot. + spin rc.' were estimated. The difference between observed and corrected is estimated as error in percent (%). We show this in Equation 10, where it is using the calculations for the 'rot. + spin rc.' angles as an example.

$$error_E^{'rot.+spin\ rc.'} = \frac{\max('rot'_E -' rot. + spin\ rc.'_E)}{\max('rot'_E)} \tag{10}$$

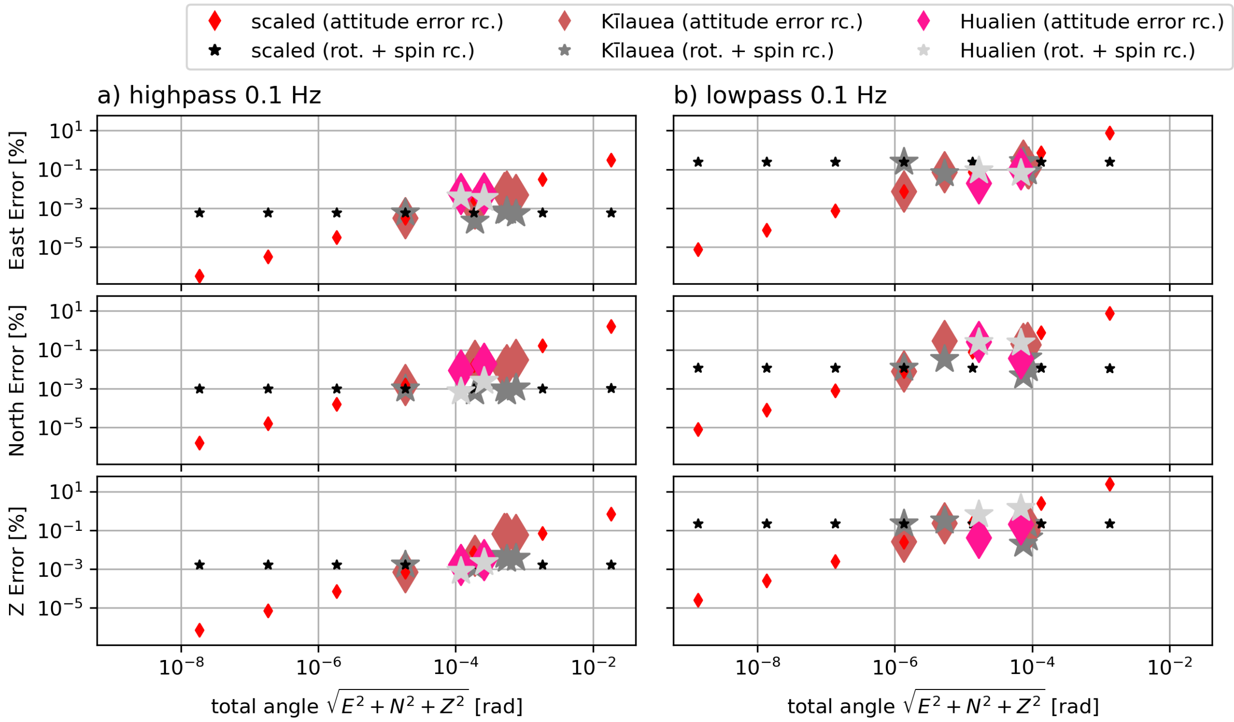

Figure 5 A summary of the effect of the two rotation errors; attitude error (diamond) and Earth's spin leakage (star), for varying rotation amplitudes. The difference between the observed and corrected are shown as error in percent (%) plotted against the total angle amplitude. The timeseries of the Ml 3.18 earthquake were scaled before estimating the influence of the two errors on the data. The error distribution for these scaled events is shown with the small markers. Each of the big markers shows the maximum error of either, real earthquakes (Ml 3.18, Ml 4.36, Mw 7.4), or three summit collapses (Mw 5.3 each). In the case of the Mw 7.4, there are data from the two stations NA01 and MDSA0. The effect is shown for both the low frequencies and the high frequencies individually.

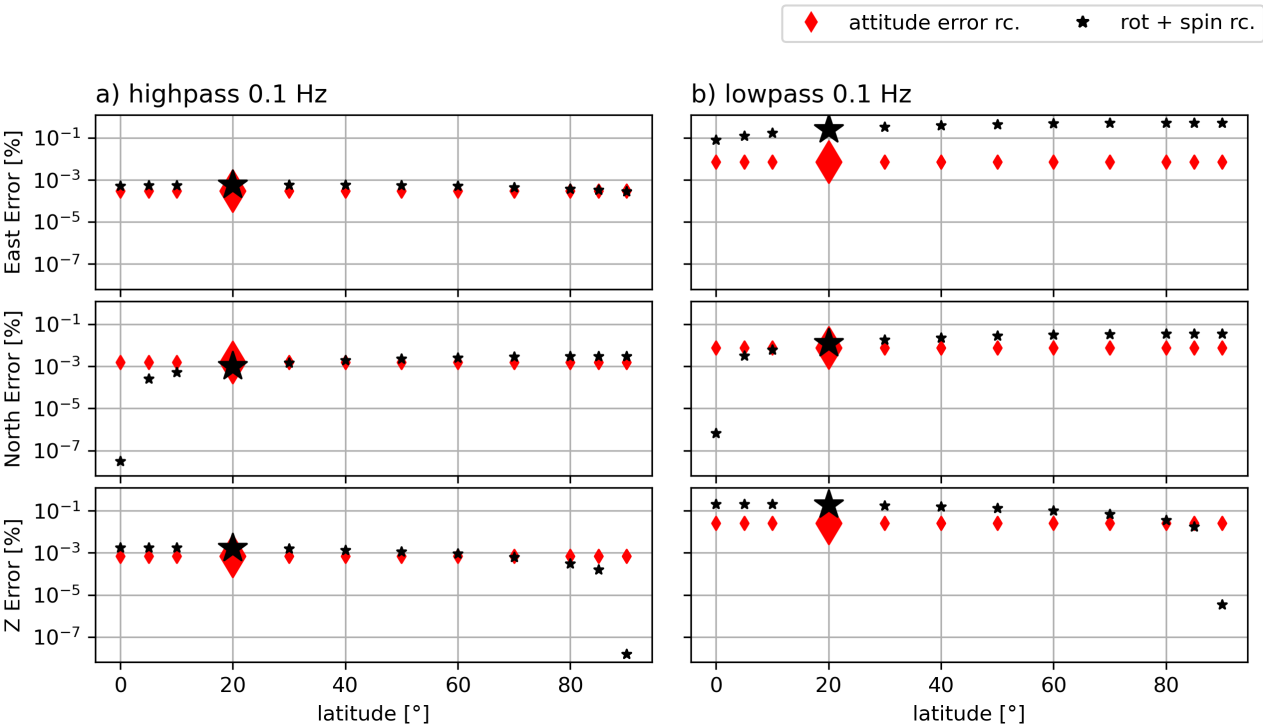

Figure 6 A summary of the effect of the stations' latitude on the two rotation errors (attitude error; star, and Earth's spin leakage; diamond). The maximum error for Ml 3.18 for the original latitude is shown with a big marker, while the smaller markers are the maximum errors from the simulated latitudes. The effect is shown for both the low frequencies and the high frequencies individually.

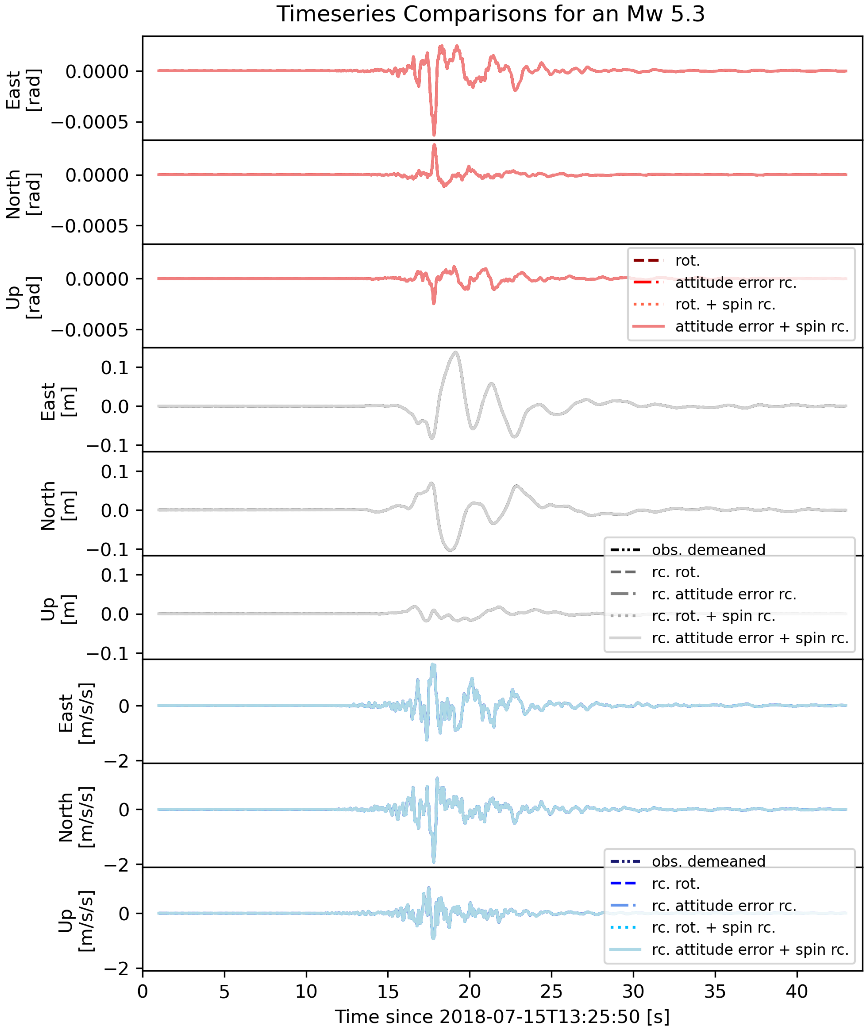

Figure 7 A Mw 5.3 summit collapse at Kīlauea Volcano on 2018-07-15T13:25:50 UTC using a highpass filter. Top subfigures show the timeseries of the four versions of the angles; uncorrected and three rotation corrected versions. The middle subfigures show the displacement, applying either demeaning or rotation-correction using each of the four angles from above. The bottom subfigures show the same but for acceleration.

As mentioned before, the rotation-induced errors are dependent on the amplitude of all three axes. Therefore, we compare the errors in percent to the total angle calculated with Equation 11.

$$max(total\ angle) = \sqrt{\begin{aligned}&\max(abs('rot'_E))^2\\&+\max(abs('rot'_N))^2\\&+\max(abs('rot'_Z))^2\end{aligned}} \quad (11)$$

The up and down scaling visualized in Figure 5 shows that the error in percent of the Earth's spin leakage stays constant, independent of the amplitude of the signal. Nonetheless, the three components East, North, and Up do not all show the exact same error, which is due to the relative angle amplitude distribution between the three axes. However, if the relative angle amplitude distribution stays the same, as is the case with our scaling, the error in percent remains the same as well. In contrast, the attitude error in percent increases when the amplitudes are increased, which is as expected. The observed Mw 5.3 summit collapses show similar behaviour as the scaled earthquake; attitude error is larger than the Earth's spin leakage. However, the match is not perfect and this is due to the fact that the error does not only depend on the amplitude of the component of interest, but it also depends on the relative angle amplitude distribution of the three components. The two recordings from the Mw 7.4 in Hualien do not match the scaling as well as the other events. Especially the North and Up component for the lower frequencies are showing the opposite trend as the scaling (see Figure 5b). In general though, the lower frequencies have a higher error for the same mean amplitude, as seen at 10^{-3} rad on the x-axis. This is most probably due to the integration process. The linear scaling shows that an increase of the amplitude by one order of magnitude will increase the error in percent by an order of magnitude as well. With some of the Mw 5.3 and the Mw 7.4 having a 1% error, these errors could become problematic when recording even larger earthquakes in the very near-field.

The Earth's spin leakage is also latitude dependent and each component reacts differently when changing the location on the Earth. Changing the latitude shifts the amount of Earth's spin that is recorded on the North and Up component, while the East component in the lo-

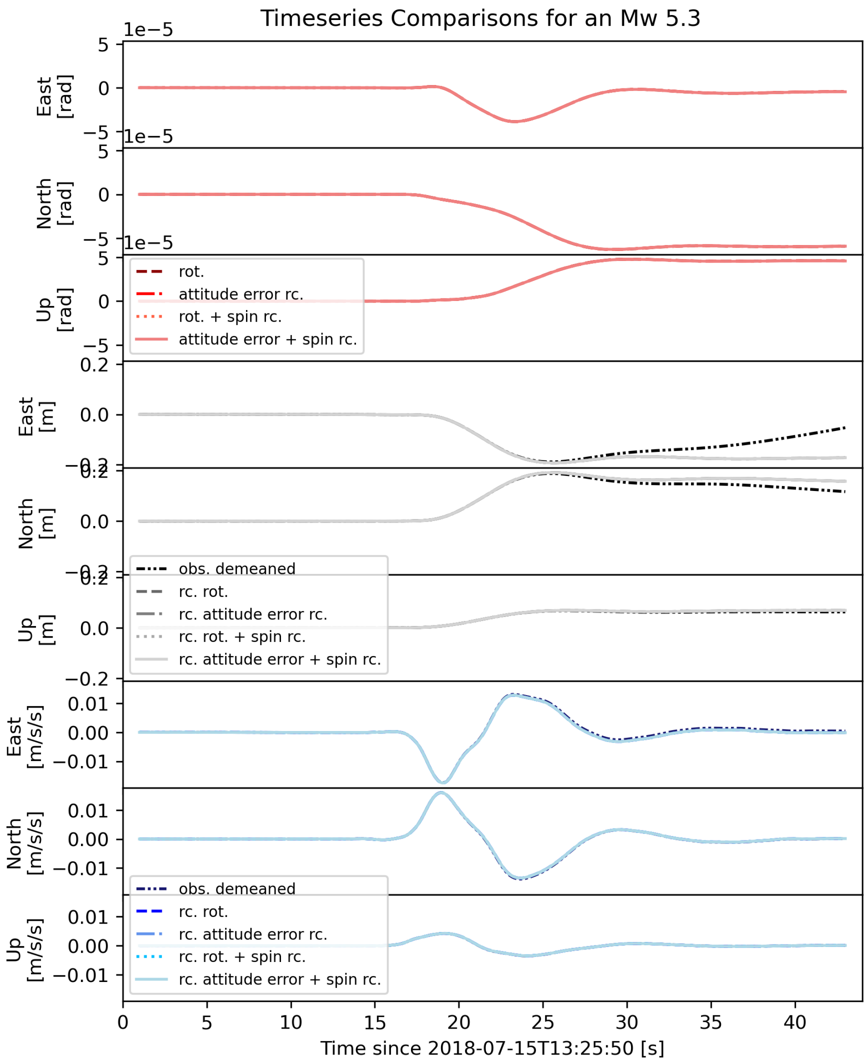

Figure 8 A Mw 5.3 summit collapse at Kīlauea Volcano on 2018-07-15T13:25:50 UTC using a lowpass filter. Top subfigures show the timeseries of the four versions of the angles; uncorrected and three rotation corrected versions. The middle subfigures show the displacement, applying either demeaning or rotation-correction using each of the four angles from above. The bottom subfigures show the same but for acceleration.

cal system does not record the Earth's spin. However, if there is a misorientation of the sensor and the sensor system no longer aligns with the local system, it will record some of the Earth's spin on the East component, especially at the North pole (90° latitude). Figure 6 shows how the error changes, when the latitude of the station is changed. The original error in percent for the Ml 3.18 at the original location is shown with the large marker. Then we assumed a latitude of 0 to 90° and estimated the error due to the attitude error and the Earth's spin correction. In Figure 6a, one can see that the attitude error is not affected as it is not influenced by the Earth's spin, so the error stays the same independent of latitude. For the Earth's spin leakage each component reacts completely differently, but the high and low frequencies have the same trend, even if the amplitudes are different. The largest error for this earthquake would be in the low frequencies at high latitudes in the East direction with $0.5\ \%$ (see Figure 6b).

4.1 Influence on acceleration and displacement

The error due to the two rotation-corrections for the rotational sensor could also influence the rotation-correction of the accelerometer sensor. Here we show how much each correction influences the accelerations and the displacements derived thereof. One Mw 5.3 is shown in detail in Figure 7 and 8. See Figures S1-S8 for a timeseries of all the other earthquakes and summit collapses. For the highpass filtered timeseries shown in Figure 7 all of the solutions look exactly the same, even though a minimal difference exists, as seen for the angles in Figure 4. However, for the lowpass filtered time series in Figure 8 there is a clear difference visible in the displacements. The rotation-correction shown as the light solid line varies from the demeaned solution. The East and North components look much more realistic, showing a constant offset after rotation-correction. However, it does not seem to matter which of the four rotation-corrections is applied, as all of them plot on top of each other.

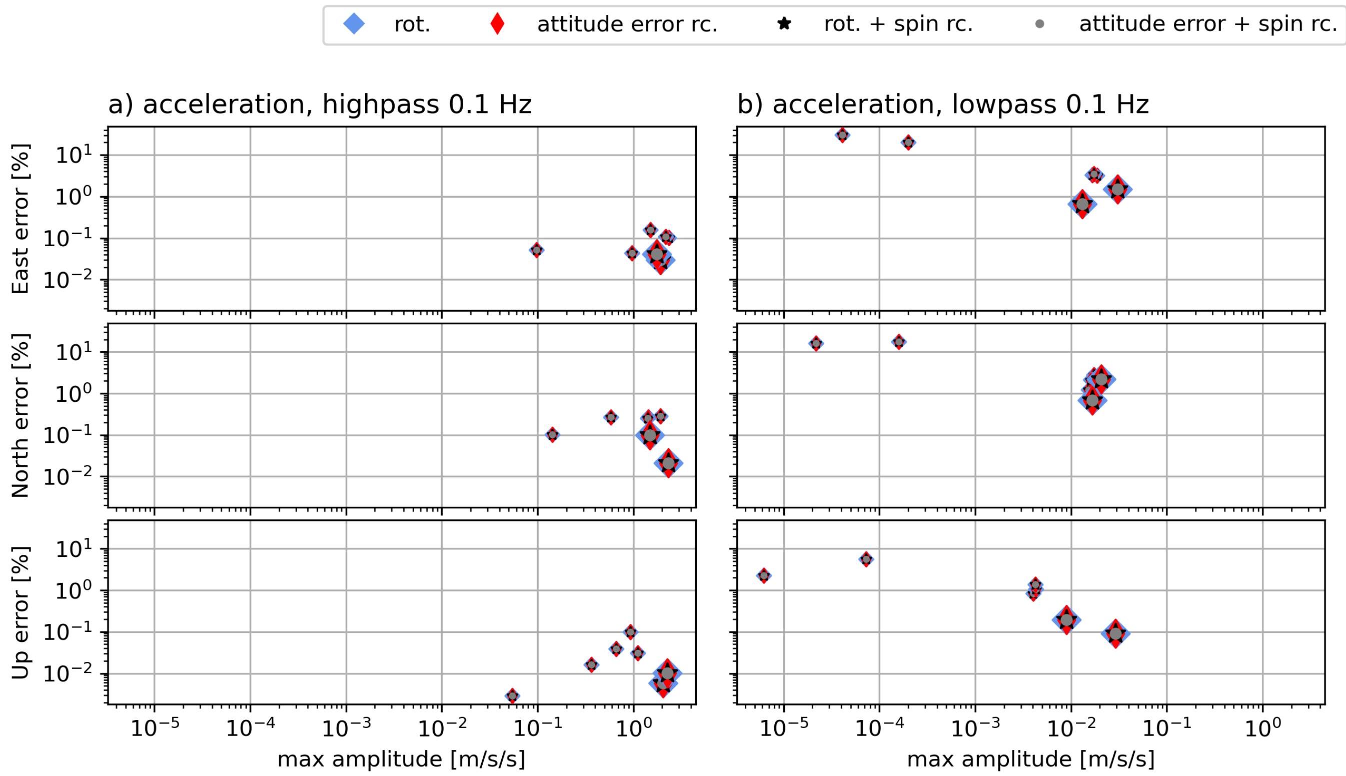

Figure 9 Summary of the different errors on the acceleration timeseries of seven earthquake recordings, visualized as maximum error in percent compared to the demeaned recording. The high frequencies are shown in (a) and the low frequencies are shown in (b). The large markers are from the Hualien Mw 7.4 event while the small markers are from the Kīlauea events.

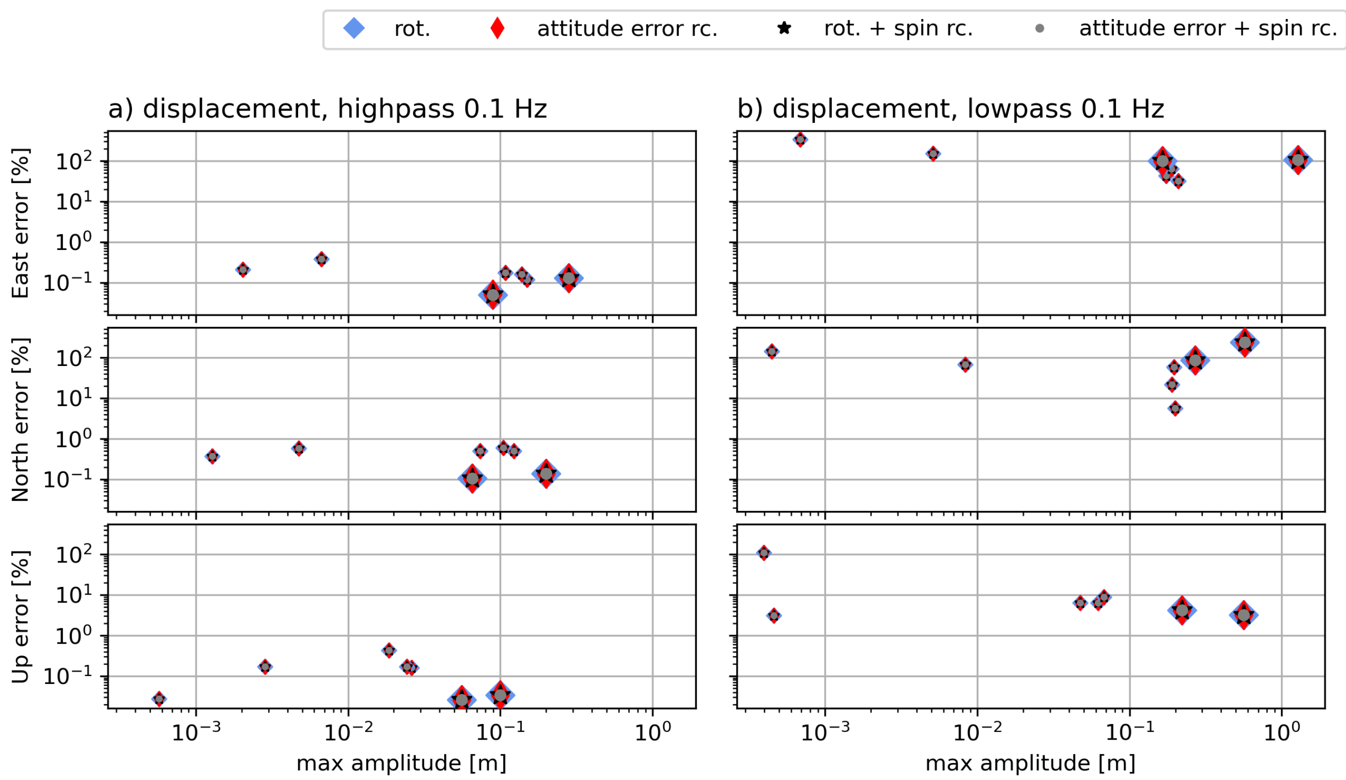

Figure 10 Summary of the different errors on the displacement timeseries of seven earthquake recordings, visualized as maximum error in percent compared to the demeaned recording. The high frequencies are shown in (a) and the low frequencies are shown in (b). The large markers are from the Hualien Mw 7.4 event while the small markers are from the Kīlauea events.

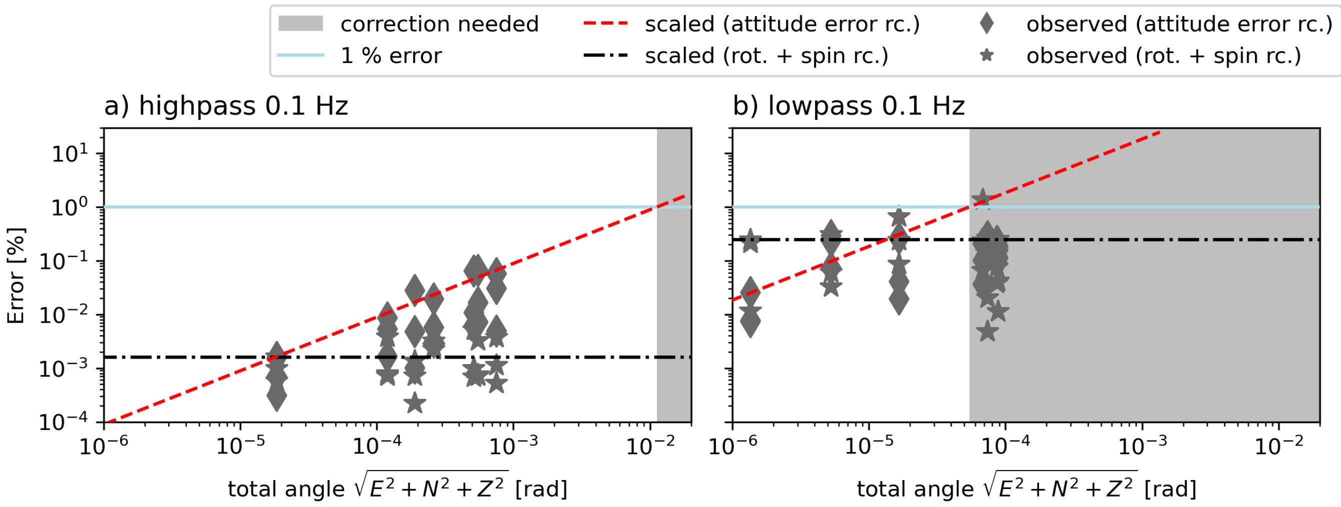

Figure 11 A guide to facilitate the decision of correcting rotational data for rotation-induced errors. The 'attitude error rc.' and the 'rot. + spin rc.' error acquired through scaling are shown in the dashed and dashed-dotted lines respectively. The observation of these two errors for all three axes East, North, and Up are shown as the diamonds and stars. The shaded area shows where the expected rotation-induced errors exceeds 1% and therefore a rotation-correction is needed. The effect is shown for both the low frequencies and the high frequencies individually.

To analyse all five earthquakes shown in Figure 5, we applied the different rotation-correction schemes to the acceleration time series and integrated twice. We then calculated the error in percent to the demeaned time series for both acceleration and displacement (Figure 9 for acceleration and Figure 10 for displacement). The high frequencies in the accelerations show errors below 0.3%, while the errors in the displacements are slightly higher, but generally the error stays below 1%, seemingly negligible. However, the low frequencies show an error of up to 20% for the accelerations and $> 300\%$ for the displacements. Again here the high displacement errors for the lower frequencies are due to the double integration. This can be seen in Figures S2, S4, S6, S8, where it is visible that there is no stable offset after the events.

5 Discussion

In this study, we have quantified 1) the percentage of error for two rotation-induced errors associated with rotational sensors and 2) explored their implications for rotation-corrections on accelerometers. While corrections for both attitude error and Earth's spin are well-established in navigation solutions, they have not been applied to seismic recordings. The community has been aware of attitude corrections due to Lin et al. (2010), but this error has not been quantified before. Our results indicate that the Earth's spin leakage in percent remains constant independent of the amplitude of the ground-motion, while the attitude error increases with increasing amplitude and becomes the dominant error above 10^{-4} rad of the total angle (as defined in Equation 11). Both errors are present across the full frequency range. The Earth's spin leakage is low enough, at about 10^{-3} % for the high frequency range to be considered negligible. However, during the Mw 7.4, the Earth spin error is almost 1% for low frequencies. On the other hand, the attitude error increases with amplitude and could pose a problem for earthquakes larger than Mw 5.3 in the near-field, or a Mw 7.4 at close distance. At a total angle of 10^{-2} rad, there is a 1 % error in the rotation data for high frequencies, which increases tenfold for low frequencies.

We cannot test how the scaled rotations impact the correction of the acceleration data, since translations and rotations cannot be scaled linearly. Additionally, the local near-surface structure might increase the rotation amplitude, without a corresponding linear increase of the translations in the wave field. Our dataset is limited to earthquakes in the near field, with no comparable data available for larger earthquakes as close to the epicenter.

For all the earthquakes we analyzed, it did not matter if we used the rotation corrected angles or uncorrected angles when applying the rotation-correction for the accelerations. The difference between the two is too small to have an influence on the accelerations or the derived displacements. However, we do find that, in general, the influence of the rotation-correction of the accelerations is as significant as demeaning at lower frequencies. Both demeaning and rotation-correction are thus necessary to retain the true ground-motion. For higher frequencies, the rotation-induced error on the displacements remained below 0.43%, which is negligible for these earthquakes. Therefore, it is not a concern in our current study.

Applying a rotation correction for rotation data becomes relevant for larger angle amplitudes, $> 10^{-2}$ rad for high frequencies, and $> 5 * 10^{-5}$ rad for low frequencies. Above this range, it is recommended to apply a rotation-correction to the observed rotations, as an error of *ca* 1% can be expected (see Figure 11). The rotation-correction of accelerations is generally advised, as especially the lower frequencies are highly contaminated due to gravitational leakage. This error is enhanced $10 - 100$ times when integration to displacement is applied. However, as seen in the rotation-corrected displacements, it is imperative that the two sensors, the rotational sensor and the accelerometer, be on the same concrete slab and bolted to the ground. Otherwise, the sensors do not observe the same part of the wave field at the same time. In fact, full navigation-style sensor correction will only be possible once all 6C are mounted in one sensor, which should be the vision for future instrumentation developments.

6 Conclusion

In conclusion, we were able to quantify the error of dynamic attitude error and Earth's spin leakage on the rotational sensor for ground-motions ranging from $10^{-6}\,rad$ to $10^{-3}\,rad$ of total angle. Through scaling, this range was broadened to $10^{-8}\,rad$ to $10^{-2}\,rad$ of total angle. In addition, the rotation-induced error on accelerations and the derived displacements were quantified, using the two unique 6C datasets at Kīlauea Volcano Hawai'i, USA and Hualien, Taiwan. We can conclude, that the rotation-induced errors on rotation sensors are less significant than initially anticipated and can be neglected for small ground-motion amplitudes. However, caution is warranted for larger amplitudes, particularly in the near-field of epicenters, where correction may be necessary. For those investigating very small changes in the signal, this correction might be necessary even for smaller amplitudes.

Acknowledgements

This study is funded through Yara Rossi by the Swiss National Science Foundation within the project P500PN_217932 'Towards a quantification of rotational motion in a seismic wave field: theory vs observation.'. We want to thank Paula Koelemeijer and an anonymous reviewer for their insightful comments that significantly improved the manuscript.

Data and code availability

The data from the Uwekahuna station vault of the Hawai'ian Volcano Observatory monitoring network at the Kīlauea Caldera on the Island of Hawai'i is openly available (USGS Hawaiian Volcano Observatory , HVO) and was first published through Wassermann et al. (2020). The recordings of the Mw 7.4 at the two stations NA01 and MDSA0 in Taiwan are available in a Zenodo folder (Lin, 2024). All of the codes used in this study, including how to download the Kīlauea dataset, are openly available in a GitHub repository Rossi (2025).

Competing interests

The authors declare no competing interests.

References

Bernauer, F., Wassermann, J., and Igel, H. Rotational sensors-a comparison of different sensor types. *Journal of Seismology*, 16 (4):595–602, 2012. doi: 10.1007/s10950-012-9286-7.

Bernauer, F., Wassermann, J., Guattari, F., Frenois, A., Bigueur, A., Gaillot, A., de Toldi, E., Ponceau, D., Schreiber, U., and Igel, H. BlueSeis3A: Full Characterization of a 3C Broadband Rotational Seismometer. *Seismological Research Letters*, 89(2A):620–629, 3 2018. doi: 10.1785/0220170143.

Bernauer, F., Wassermann, J., and Igel, H. Dynamic Tilt Correction Using Direct Rotational Motion Measurements. *Seismological Research Letters*, 91(5):2872–2880, 9 2020. doi: 10.1785/0220200132.

Bernauer, F., Behnen, K., Wassermann, J., Egdorf, S., Igel, H., Donner, S., Stammler, K., Hoffmann, M., Edme, P., Sollberger, D., Schmelzbach, C., Robertsson, J., Paitz, P., Igel, J., Smolinski, K., Fichtner, A., Rossi, Y., Izgi, G., Vollmer, D., Eibl, E. P., Buske, S., Veress, C., Guattari, F., Laudat, T., Mattio, L., Sèbe, O., Olivier, S., Lallemand, C., Brunner, B., Kurzych, A. T., Dudek, M., Jaroszewicz, L. R., Kowalski, J. K., Bońkowski, P. A., Bobra, P., Zembaty, Z., Vackář, J., Málek, J., and Brokesova, J. Rotation, strain, and translation sensors performance tests with active seismic sources. *Sensors*, 21(1):1–23, 2021. doi: 10.3390/s21010264.

Brokesova, J. and Malek, J. Rotaphone, a Self-Calibrated Six-Degree-of-Freedom Seismic Sensor and Its Strong-Motion Records. *Seismological Research Letters*, 84(5):737–744, 9 2013. doi: 10.1785/0220120189.

Brotzer, A., Igel, H., Bernauer, F., Wassermann, J., Mellors, R., and Vernon, F. On single-station, six degree-of-freedom observations of local to regional seismicity at the Piñon Flat Observatory in Southern California. *Seismica*, 4(1), 5 2025. doi: 10.26443/seismica.v4i1.1416.

Chen, C., Wang, Y., Sun, L., Lin, C. J., Wei, Y., Liao, C., Lin, B., and Qin, L. Six-Component Earthquake Synchronous Observations Across Taiwan Strait: Phase Velocity and Source Location. *Earth and Space Science*, 10(12), 12 2023. doi: 10.1029/2023EA003040.

Clinton, J. F. and Heaton, T. H. Potential Advantages of a Strong-motion Velocity Meter over a Strong-motion Accelerometer. *Seismological Research Letters*, 73(3):332–342, 5 2002. doi: 10.1785/gssrl.73.3.332.

Crawford, W. C. and Webb, S. C. Identifying and removing tilt noise from low-frequency (\<0.1 Hz) seafloor vertical seismic data. *Bulletin of the Seismological Society of America*, 90(4):952–963, 2000. doi: 10.1785/0119990121.

De Ridder, S. A. and Curtis, A. Seismic gradiometry using ambient seismic noise in an anisotropic Earth. *Geophysical Journal International*, 209(2):1168–1179, 5 2017. doi: 10.1093/gji/ggx073.

Diebel, J. Representing Attitude: Euler Angles, Unit Quaternions, and Rotation Vectors. 11 2006.

Draper, C. S. Origins of inertial navigation. *Journal of Guidance and Control*, 4(5):449–463, 9 1981. doi: 10.2514/3.19748.

Euler, L. Nova methodus motum corporum rigidorum determinandi. *Novi Commentari Academiae Scientiarum Imperalis Petropolitanae*, 20:208–238, 1775.

Geng, J., Wen, Q., Chen, Q., and Chang, H. Six-Degree-of-Freedom Broadband Seismogeodesy by Combining Collocated High-Rate GNSS, Accelerometers, and Gyroscopes. *Geophysical Research Letters*, 46(2):708–716, 1 2019. doi: 10.1029/2018GL081398.

Graizer, V. Tilts in strong ground motion. *Bulletin of the Seismological Society of America*, 96(6):2090–2102, 2006. doi: 10.1785/0120060065.

Hasan, A., Samsudin, K., and Rahman bin Ramli, A. A Review of Navigation Systems (Integration and Algorithms). *Australian Journal of Basic and Applied Sciences*, 3(2):943–959, 2009. https://www.researchgate.net/publication/269990234.

Ichinose, G. A., Ford, S. R., and Mellors, R. J. Regional Moment Tensor Inversion Using Rotational Observations. *Journal of Geophysical Research: Solid Earth*, 126(2), 2 2021. doi: 10.1029/2020JB020827.

Kalman, R. E. A New Approach to Linear Filtering and Prediction Problems 1. *Journal of Basic Engineering*, pages 35–45, 1960. doi: 10.1115/1.3662552.

Kurzych, A., Kowalski, J. K., Sakowicz, B., Krajewski, Z., and Jaroszewicz, L. R. The laboratory investigation of the innovative sensor for torsional effects in engineering structures' monitoring. *Opto-Electronics Review*, 3(24):134–43, 2016. doi: 10.1515/oere−2016−0017.

Lin, C.-J. 6C dataset for Mw 7.4 Hualien earthquake on 2024-04-02 at station locations MDSA0 and NA01., 2024. doi: 10.5281/zenodo.13653585.

Lin, C.-J., Huang, H.-P., Liu, C.-C., and Chiu, H.-C. Application of Rotational Sensors to Correcting Rotation-Induced Effects on Accelerometers. *Bulletin of the Seismological Society of America*, 100(2):585–597, 4 2010. doi: 10.1785/0120090123.

Lindner, F., Wassermann, J., Schmidt-Aursch, M. C., Schreiber, K. U., and Igel, H. Seafloor Ground Rotation Observations: Potential for Improving Signal-to-Noise Ratio on Horizontal OBS Components. *Seismological Research Letters*, 88(1):32–38, 2017. doi: 10.1785/0220160051.

Ma, K.-F., von Specht, S., Kuo, L.-W., Huang, H.-H., Lin, C.-R., Lin, C.-J., Ku, C.-S., Wu, E.-S., Wang, C.-Y., Chang, W.-Y., and Jousset, P. Broad-band strain amplification in an asymmetric fault zone observed from borehole optical fiber and core. *Communications Earth & Environment*, 5(1):402, 7 2024. doi: 10.1038/s43247-024-01558-6.

Pancha, A., Webb, T. H., Stedman, G. E., McLeod, D. P., and Schreiber, K. U. Ring laser detection of rotations from teleseismic waves. *Geophysical Research Letters*, 27(21):3553–3556, 11 2000. doi: 10.1029/2000GL011734.

Rossi, Y. *Next Generation Monitoring of Strong Ground Motions and Structural Vibrations - Combining Accelerometer, GNSS and Rotation Sensors*. PhD thesis, ETH Zürich, 2023. doi: 10.3929/ethz-b-000645882.

Rossi, Y. YaraRossi/QuantifyRotationErrors: Code for: Quantifying Rotation-Induced Errors in Near-Field Seismic Recordings: Assessing Impact on Rotation and Acceleration Measurements. (v1.0.2)., 2025. doi: 10.5281/zenodo.15387179.

Rossi, Y., Tatsis, K., Awadaljeed, M., Arbogast, K., Chatzi, E., Rothacher, M., and Clinton, J. Kalman Filter-Based Fusion of Collocated Acceleration, GNSS and Rotation Data for 6C Motion Tracking. *Sensors*, 21(4):1543, 2 2021. doi: 10.3390/s21041543.

Rossi, Y., Tatsis, K., Hohensinn, R., Clinton, J., Chatzi, E., and Rothacher, M. Unscented Kalman Filter–Based Fusion of GNSS, Accelerometer, and Rotation Sensors for Motion Tracking. *Journal of Structural Engineering*, 150(7), 7 2024. doi: 10.1061/JSENDH.STENG-12872.

Savage, P. G. *Strapdown analytics*. Strapdown Associates, 2000.

Sollberger, D., Greenhalgh, S. A., Schmelzbach, C., Van Renterghem, C., and Robertsson, J. O. A. 6-C polarization analysis using point measurements of translational and rotational ground-motion: theory and applications. *Geophysical Journal International*, 213(1):77–97, 4 2018. doi: 10.1093/gji/ggx542.

U.S. Geological Survey. M7.4 - 15 km S of Hualien City, Taiwan, Finite Fault, 8 2024. https://earthquake.usgs.gov/earthquakes/eventpage/us7000m9g4/finite-fault?source=us&code=us7000m9g4_1.

USGS Hawaiian Volcano Observatory (HVO), U. S. o. A. Hawaiian Volcano Observatory Network (HVO), 1956.

Venkateswara, K., Paros, J., Bodin, P., Wilcock, W., and Tobin, H. J. Rotational Seismology with a Quartz Rotation Sensor. *Seismological Research Letters*, 93(1):173–180, 1 2021. doi: 10.1785/0220210171.

Wassermann, J., Bernauer, F., Shiro, B., Johanson, I., Guattari, F., and Igel, H. Six-Axis Ground Motion Measurements of Caldera Collapse at Kīlauea Volcano, Hawai'i—More Data, More Puzzles? *Geophysical Research Letters*, 47(5):1–7, 3 2020. doi: 10.1029/2019GL085999.

Yuan, S., Gessele, K., Gabriel, A. A., May, D. A., Wassermann, J., and Igel, H. Seismic Source Tracking With Six Degree-of-Freedom Ground Motion Observations. *Journal of Geophysical Research: Solid Earth*, 126(3), 3 2021. doi: 10.1029/2020JB021112.